PHYSICAL REVIEW D **88,** 054504 (2013)

Inside the SU(3) quark-antiquark QCD flux tube: Screening versus quantum widening

N. Cardoso,* M. Cardoso,† and P. Bicudo‡

Departamento de Física, CFTP, Instituto Superior Técnico, Avenida Rovisco Pais, 1049-001 Lisboa, Portugal

(Received 14 February 2013; published 13 September 2013)

In lattice QCD, color confinement manifests in flux tubes. We compute in detail the quark-antiquark flux tube for pure gauge SU(3) dimension $D = 3 + 1$ for quark-antiquark distances R ranging from 0.4 to 1.4 fm. To increase the signal-to-noise ratio, we apply the improved multihit and extended smearing techniques. We detail the gauge-invariant squared components of the color electric and color magnetic fields both in the mediator plane between the static quark and static antiquark and in the planes of the charges. We fit the field densities with appropriate *Ansätze*, and we observe the screening of the color fields in all studied planes together with the quantum widening of the flux tube in the mediator plane. All components squared of the color fields are nonvanishing and are consistent with a penetration length $\lambda \sim 0.22$ to 0.24 fm and an effective screening mass $\mu \sim 0.8$ to 0.9 GeV. The quantum widening of the flux tube is well fitted with a logarithmic law in R.

DOI: 10.1103/PhysRevD.88.054504 PACS numbers: 11.15.Ha, 11.25.−w, 12.38.Gc, 74.25.Uv

I. INTRODUCTION

Confinement in QCD remains a central problem of strong interactions. It has already been established, both from gauge-invariant lattice QCD simulations [1–4] and from experimental observations like Regge trajectories [5–9], that the quark-antiquark confining potential is linear and that a flux tube develops between quark-antiquark static charges. Even in dynamical QCD where the flux tube breaks due to the creation of another quark and antiquark, a flux tube develops up to moderate quark-antiquark distances. Recently, the flux tubes have been shown to also occur in lattice QCD simulations of different exotic hadrons [10–14]. Here we return to the fundamental quark-antiquark flux tube to measure in detail the profile of the SU(3) pure gauge lattice QCD flux tube in dimensions $D = 3 + 1$. We parametrize the flux tube profile, providing new data for a better understanding of the confinement in QCD.

In particular, presently two different perspectives for the QCD flux tube exist, possibly leading to the two different flux tubes of Fig. 1, and we quantitatively compare them.

Already in the 1970s, Nambu [15], 't Hooft [16], and Mandelstam [17] proposed that quark confinement would be physically interpreted using the dual version of the superconductivity [18,19]. The QCD vacuum state would behave like an ordinary magnetic superconductor, where Cooper-pair condensation leads to the Meissner effect, and the magnetic flux is excluded or squeezed in a quasi-one-dimensional tube, the Abrikosov vortex, where the magnetic flux is quantized topologically. Magnetic charges are confined by Abrikosov-Nielsen-Olesen vortices [20–22] in an ordinary superconductor (Meissner effect). Thus, it is important for the understanding of confinement in QCD to measure the flux tube profile and to parametrize the color screening [23–29]. Moreover, the penetration length can be related as

$$\lambda = \mu^{-1} \tag{1}$$

to a possible effective mass μ of the dual gluon if we further explore the analogy between QCD and superconductors where the field in the London equation has a direct relation with an effective mass of the interaction particle fields, i.e., the photon. The dual gluon mass has been studied by several authors [30–37], as well as the gluon effective mass, see Ref. [38] for a review of the dual gluon and gluon effective masses present in the literature. Interestingly, there is also evidence of a gluon mass in the Landau gauge [39] and in the multiplicity of particles produced in heavy ion collisions [40]. Recently, the penetration length started to be computed with gauge-invariant lattice QCD techniques [38,41,42]. In superconductors, another parameter, the coherence length ξ, is defined as well and related to the curvature of the flux tube profile.

On the other hand, at quark-antiquark distances larger than the penetration length, the flux tube is similar to a quantum string, and the quantum string vibrates even in the ground state where it has zero mode vibrations. A fair description of the fundamental QCD flux tube—with charges in the triplet representation of SU(3)—is given by the string model based on the Nambu-Goto action [43,44],

$$S = -\sigma \int d^2\Sigma. \tag{2}$$

The energy of the quantum string with length R and fixed ends with quantum transverse fluctuations quantum number n is expressed in the Lüscher term and in the Arvis potential [45,46],

*nunocardoso@cftp.ist.utl.pt
†mjdcc@cftp.ist.utl.pt
‡bicudo@ist.utl.pt

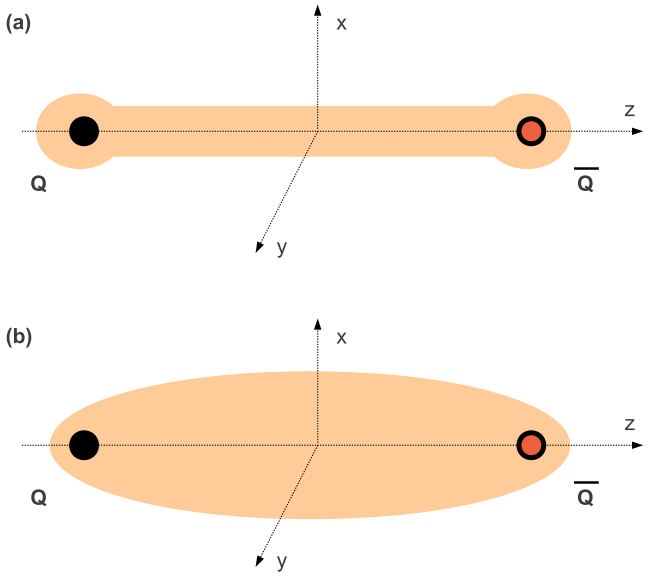

FIG. 1 (color online). In (a) we illustrate a classical flux tube similar to a solution of the Ginzburg-Landau and Ampère equations for a superconductor. In (b) we illustrate a quantum flux tube, as in a lattice QCD simulation, where the widening of the flux tube occurs due to the zero mode string vibration. The squeezing of the flux tube due to the color screening in (a) is masked by the widening in (b).

$$V_n(R) = \sigma\sqrt{R^2 + \frac{2\pi}{\sigma}\left(n - \frac{D-2}{24}\right)} = \sigma R + \frac{\pi}{R}\left(n - \frac{D-2}{24}\right) + \cdots \tag{3}$$

In Eq. (3), D is the dimension of the spacetime. Note that the Arvis potential is tachyonic at small distances since the argument of the square root is negative; moreover, rotational invariance is only achieved for $D = 26$. Nevertheless, the first two terms in the $1/R$ expansion are more general that the Arvis potential, since they fit the $D = 3$ and $D = 4$ lattice data quite well beyond the tachyonic distance. The $1/R$ term is independent of the string tension σ and for the physical $D = 3 + 1$ it has the value $-\frac{\pi}{12}$. This is the Lüscher term [45]. The energy spectrum of a static quark-antiquark and of its flux tube is certainly well defined (not tachyonic), and this was the first evidence of flux tube vibrations found in lattice field theory. Moreover, it was shown [45] that the width of the ground-state flux tube diverges when $R \to \infty$ with a logarithmic law,

$$w^2 \sim w_0^2 \log\frac{R}{R_0}, \tag{4}$$

where w^2 is the mean squared radius of the flux tube. This enhancement of the flux tube transverse radius as $R \to \infty$ is called widening. The widening as been recently extended with two-loop calculations [47]. The flux tube widening has been verified numerically for compact U(1) QED $D = 2 + 1$ lattices [48], for non-Abelian SU(2) $D = 2 + 1$ lattices [49–65] and, more recently, for the more physical four-dimensional SU(3) case [66,67].

In this paper, we present an SU(3) gauge-independent lattice QCD computation in $D = 3 + 1$ for the penetration length and for the string quantum widening. Although this work is not the first one to study the widening in SU(3) for a spacetime dimension of $D = 3 + 1$, we think it is the first attempt to separate the screening from the quantum widening. While the screening leads to an exponential decay of the flux tube profile, the widening leads to a Gaussian profile.

In Sec. II, we introduce the lattice QCD formulation. We briefly review the Wilson loop for this system, which was used by Bicudo *et al.* [68] and Cardoso *et al.* [10,69], and show how we compute the color fields and the Lagrangian and energy densities' distributions. In Sec. III, we show the techniques we utilize to increase the signal-to-noise ratio. In Sec. IV, we discuss our *Ansatz* for the width of the QCD flux tube. In Sec. V, the lattice numerical results are shown together with their fits. Finally, we present the conclusion in Sec. VI.

II. COMPUTATION OF THE CHROMOFIELDS IN THE FLUX TUBE

We impose our static quark-antiquark system with the standard Wilson $W(R, T)$ loop [70],

$$\begin{aligned} W(R,T) = \mathrm{Tr}\Big[& U_\mu\Big(0,0,\frac{-R}{2},\frac{-T}{2}\Big)\ldots U_\mu\Big(0,0,\frac{R}{2}-1,\frac{-T}{2}\Big) \\ & \times U_4\Big(0,0,\frac{R}{2},\frac{-T}{2}\Big)\ldots U_4\Big(0,0,\frac{R}{2},\frac{T}{2}-1\Big) \\ & \times U_\mu^\dagger\Big(0,0,\frac{R}{2}-1,\frac{T}{2}\Big)\ldots U_\mu^\dagger\Big(0,0,\frac{-R}{2},\frac{T}{2}\Big) \\ & \times U_4^\dagger\Big(0,0,\frac{-R}{2},\frac{T}{2}-1\Big)\ldots U_4^\dagger\Big(0,0,\frac{-R}{2},\frac{T}{2}-1\Big)\Big]. \end{aligned} \tag{5}$$

In the limit of large Euclidean time limit $T \to \infty$, the expectation value

$$\langle W(R,T)\rangle = \sum_n |C_n|^2 e^{-V_n T} \tag{6}$$

selects the ground state of the static quark-antiquark system aligned in the z direction with an intercharge distance R.

To compute the gauge-invariant squared components of the chromoelectric and chromomagnetic fields on the lattice, we utilize the Wilson loop and plaquette $P_{\mu\nu}$ expectation values,

$$\langle B_i{}^2(\mathbf{r})\rangle = \frac{\langle W(R,T)P(\mathbf{r})_{jk}\rangle}{\langle W(R,T)\rangle} - \langle P(\mathbf{r})_{jk}\rangle,$$
$$\langle E_i{}^2(\mathbf{r})\rangle = \langle P(\mathbf{r})_{0i}\rangle - \frac{\langle W(R,T)P(\mathbf{r})_{0i}\rangle}{\langle W(R,T)\rangle}, \quad (7)$$

where the jk indices of the plaquette complement the index i of the magnetic field. The plaquette at position $\mathbf{r} = (x, y, z)$ is computed at lattice Euclidean time $t = 0$, as depicted in Fig. 2. In Eq. (7), we subtract from the plaquette computed in the presence of the static charges, the average plaquette computed in the vacuum. This cancels the vacuum fluctuations of the fields. To get the plaquette in the lattice vertices, we average the neighboring plaques.

We define our plaquette as

$$P_{\mu\nu}(\mathbf{r}) = 1 - \frac{1}{3}\,\mathrm{Re\,Tr}[U_\mu(\mathbf{r})U_\nu(\mathbf{r}+\mu)U_\mu^\dagger(\mathbf{r}+\nu)U_\nu^\dagger(\mathbf{r})], \quad (8)$$

which for small lattice spacing a can be expanded in a series of powers of the symmetric tensor $F^{\mu\nu\,c}$ whose components are the electric and magnetic field components. Prior to performing the trace, the expansion reads [71,72]

$$\begin{aligned} P_{\mu\nu} &= 1 - \frac{1}{3}\,\mathrm{Re\,Tr}\exp\left[iga^2\sum_c F^c_{\mu\nu}T^c + \mathcal{O}(a^3)\right] \\ &= \mathrm{Re\,Tr}\Big\{\frac{1}{36}g^2a^4[F^c_{\mu\nu}F^c_{\mu\nu} + \mathcal{O}(a)]I \\ &\quad - \frac{i}{3}ga^2\sum_c[F^c_{\mu\nu} + \mathcal{O}(a)]T^c\Big\}, \end{aligned} \quad (9)$$

where $T^c = \lambda^c/2$ are the generators of the Lie algebra and I is the identity matrix. In Abelian theories, such as U(1) QED, the electric and magnetic field components can be computed with the plaquette at order a^2 and are gauge invariant. In non-Abelian gauge theories, such as SU(3), the electric and magnetic field components are not gauge invariant since they depend on the color index c. In SU(3), we have to go up to order a^4 to find our first nonvanishing gauge-invariant term in the plaquette expansion, and it is the square of a component of the electric or magnetic fields. For instance $E_x{}^2 = \sum_c (E_x{}^c)^2$ is gauge invariant, while $E_x{}^c$ is not. Thus, to directly produce the squared components, we perform the trace.

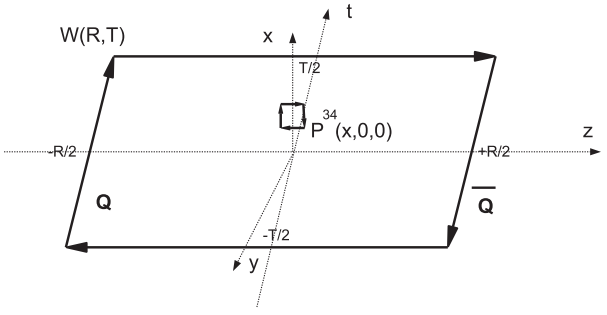

FIG. 2. Wilson loop and example of a plaquette for the computation of the electric field squared, where we project the $D = 3 + 1$ spacetime in a plane including the z axis. We compute the fields squared in three planes perpendicular to the charge-anticharge axis: in the mediator plane of the charges as illustrated in this figure, in the plane of the charge, and in the plane of the anticharge.

Notice the field densities defined in Eq. (7) are dimensionless. To arrive at physical units

$$\sum_c F^c_{\mu\nu}F^c_{\mu\nu} = \frac{2\beta}{a^4}\left[1 - \frac{1}{3}\,\mathrm{Tr}(P_{\mu\nu})\right] + \mathcal{O}(a), \quad (10)$$

we have to multiply the dimensionless field densities by $2\beta/a^4$.

The classical energy ($\mathcal{H}$) and the Lagrangian ($\mathcal{L}$) densities are directly computed from the filed densities,

$$\langle\mathcal{H}(\mathbf{r})\rangle = \frac{1}{2}(\langle\mathbf{E}^2(\mathbf{r})\rangle + \langle\mathbf{B}^2(\mathbf{r})\rangle), \quad (11)$$

$$\langle\mathcal{L}(\mathbf{r})\rangle = \frac{1}{2}(\langle\mathbf{E}^2(\mathbf{r})\rangle - \langle\mathbf{B}^2(\mathbf{r})\rangle), \quad (12)$$

and we can utilize any of the densities, either of the squared component of the fields, of the action, or of the classical energy, to study the profiles of the flux tubes.

III. TECHNIQUES EMPLOYED TO IMPROVE THE SIGNAL

To compute the static field expectation value, we plot the expectation value $\langle E_i^2(\mathbf{r})\rangle$ or $\langle B_i^2(\mathbf{r})\rangle$ as a function of the temporal extent T of the Wilson loop. At sufficiently large T, the ground state corresponding to the studied quantum numbers dominates, and the expectation value tends to a horizontal plateau. To compute the fields, we fit the horizontal plateaus obtained for each point $\mathbf{r}$. For the distances R considered, we find in the range of $T \in [4, 12]$ in lattice units, horizontal plateaus with a $\chi^2/\mathrm{d.o.f.} \in [0.3, 2.0]$. We finally compute the error bars of the fields with the jackknife method.

To produce the expectation values, we utilize 1100 pure gauge 32^4 configurations with $\beta = 6.0$ generated with CUDA and graphics processing units [73]. This beta corresponds to the lattice spacing $a = 0.098\,373\,7$ fm and $a^{-1} = 2.002\,57T$ GeV [74].

In order to reduce the noise, we utilize an improved version of the multihit illustrated in Fig. 3 and an extended spatial smearing technique with staples shown in Fig. 4. Moreover, to reduce the contamination of the ground state from the excited states, we use the energy gap between the first excited and ground states depicted in Fig. 5 calculated using a variational basis. With all three combined techniques, we are able to get a clear signal, with statistical errors already smaller than the lattice artifacts plotted in Fig. 6.

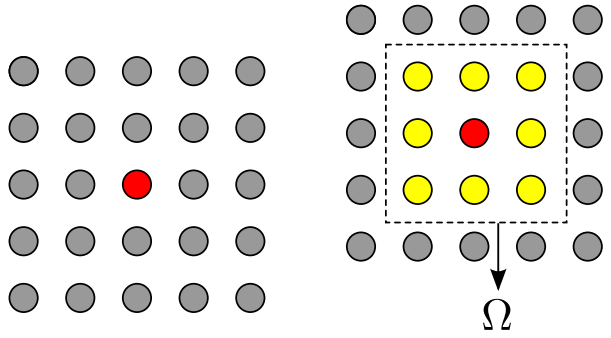

FIG. 3 (color online). Left: Simple multihit. Right: Extended multihit.

A. Extended multihit

In the multihit [75,76] method, we replace each temporal link by its thermal average, with its first neighbors fixed, that is, $U_4 \to \bar{U}_4 = \frac{\int dU_4 U_4 e^{\beta \mathrm{Tr}[U_4 F^\dagger]}}{\int dU_4 e^{\beta \mathrm{Tr}[U_4 F^\dagger]}}$.

We generalize this method by instead replacing each temporal link by its thermal average with the first N neighbors fixed, that is,

$$U_4 \to \bar{U}_4 = \frac{\int [\mathcal{D}U]_\Omega U_4 e^{\beta \sum_{\mu s} \mathrm{Tr}[U_\mu(\mathbf{s}) F^\dagger_\mu(\mathbf{s})]}}{\int [\mathcal{D}U]_\Omega e^{\beta \sum_{\mu s} \mathrm{Tr}[U_\mu(\mathbf{s}) F^\dagger_\mu]}}. \quad (13)$$

By using $N = 2$, we are able to greatly improve the signal when compared with the error reduction achieved with the simple multihit. Of course, this technique is more computer intensive than a simple multihit, while being simpler to implement than a multilevel [77] and its application being independent in the value of R. The only restriction is that $R \geq 2N$ for this technique to be valid.

B. Extended spatial smearing

To increase the ground-state overlap, we use a spatial extended APE-like smearing, first defined by the APE Collaboration [78,79], namely,

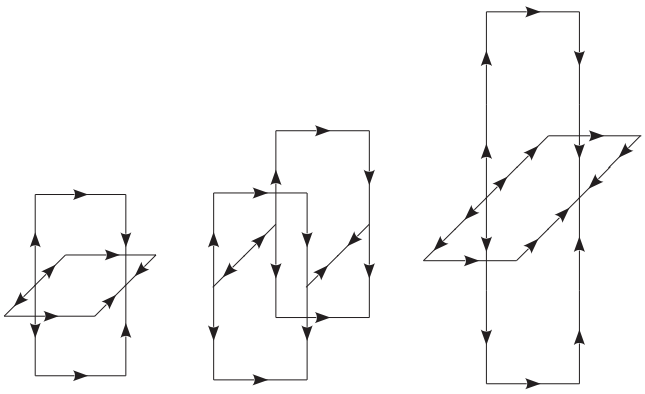

FIG. 4. Staples used in the extended spatial smearing.

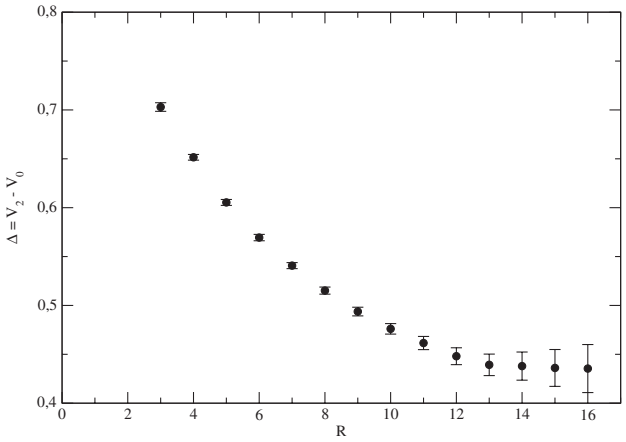

FIG. 5. Gap between the first excited state and the ground state $\Delta = V_2 - V_1$ as a function of R.

$$U_i \to \mathcal{P}_{\mathrm{SU}(3)}\left[U_i + w_1 \sum_j S^1_{ij} + w_2 \sum_j S^2_{ij} + w_3 \sum_j S^3_{ij}\right], \quad (14)$$

where the staples S^1_{ij}, S^2_{ij}, and S^3_{ij} are the ones shown in Fig. 4. As can be seen, this technique reduces to the common APE smearing when $w_2 = w_3 = 0$.

C. Variational basis to compute Δ

Even by using this technique, we were not able to find a value of t for which the plaquette to Wilson loop correlators are stable within error bars, while still having a sufficiently high signal-to-noise ratio. To solve this, we note

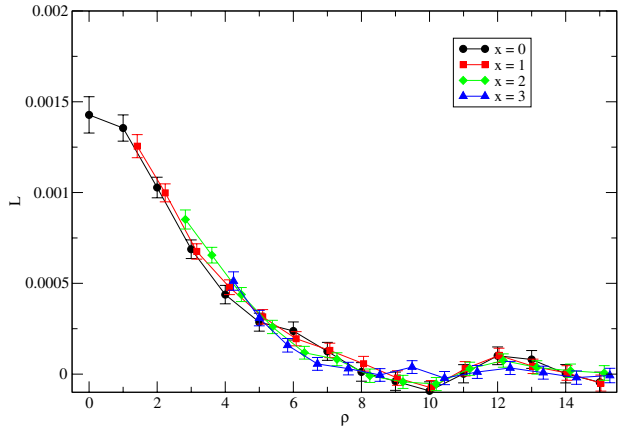

FIG. 6 (color online). Lagrangian density computed in the mediator plane for intercharge distance of $R = 12$ as a function of the cylindrical distance r. We plot separately the density measured in different lines of the mediator plane with fixed x. At large distances r, the lattice artifacts, due to the square and finite lattice, produce systematic errors already larger than the statistical error bars represented in the figure. This shows that our statistical noise is sufficiently reduced by the extended multihit, the extended spatial smearing, and the variational basis methods.

that the correlator, which gives the average of field $\langle F \rangle$, should be given by the formula $\langle F \rangle_t = \langle F \rangle_\infty + be^{-\Delta t}$ for large values of t, with $\Delta = V_2 - V_0$ being the difference between the first excited state that has overlap with the Wilson loop and the ground-state potential. To compute Δ, we a use a variational basis [80,81] of four levels of APE smearing, with the potentials V_2 and V_0 being given by the solution of the variational generalized eigensystem

$$\langle W_{ij}(t) \rangle c_j^n(t) = w_n(t) \langle W_{ij}(0) \rangle c_j^n(t), \tag{15}$$

where $\langle W_{ij} \rangle = \langle \mathcal{O}_i(t) \mathcal{O}_j^\dagger(0) \rangle$ is the correlation between the meson creation and annihilation operators at time t and 0 in the smeared states i and j, respectively.

IV. OUR *ANSÄTZE* AND THE SEPARATION OF PENETRATION LENGTH, COHERENCE LENGTH, AND QUANTUM WIDENING

A. In the mediator plane of the two static charges

In a quantum flux tube, as in the QCD flux tube, at least three parameters with the dimension of a length determine the flux tube profile in the mediator plane of the two static charges.

The width ω is a function of the flux tube length R and is partly due to the quantum widening of the flux tube produced by the zero mode quantum oscillations of the stringlike flux tube.

Moreover, the flux tube is not an ideal string, and it is due to the squeezing of the fields by the color confinement. The penetration length λ quantifies the exponential screening of the fields penetrating the medium.

But the flux tube cannot just be parametrized by the penetration length, because it should be differentiable at the center of the flux tube, with a finite curvature. For a finite curvature, we need another parameter ν.

All this is clear in Fig. 7, where we show the logarithm of the profile of the fields we compute. The logarithm is similar to a parabola at small distances and to a line at large distances. The width ω clearly depends on the intercharge distance R.

Thus, we choose a flux tube profile *Ansatz* consisting of the exponential of the simplest possible function interpolating between a parabola and a straight line. The simplest exponent we can find is inspired in the relativistic kinetic energy in order to interpolate between a Gaussian at small r and an exponential decay at large r. Utilizing the cylindrical coordinates (r, θ, z), our *Ansatz* for the profile of the quantum flux tube is

$$F_{\rm qu}{}^2(r) = F_0{}^2 \exp\left(-\frac{2}{\lambda}\sqrt{r^2+\nu^2} + 2\frac{\nu}{\lambda}\right), \tag{16}$$

where $F_{\rm qu}{}^2$ corresponds to any of the components of the squared electric or magnetic fields $E_r{}^2$, $E_\theta{}^2$, $E_z{}^2$, $B_r{}^2$, $B_\theta{}^2$, $B_z{}^2$, or to the Lagrangian density L. Our *Ansatz* is depicted in Fig. 8, and it has the same exponent as the quantum profile deduced in the model of Ref. [55]. Its series expansions for large r and for small r are, respectively,

$$\begin{aligned} F_{\rm qu}{}^2(r) &= F_0{}^2 e^{\frac{2\nu}{\lambda}} \exp\left[-\frac{2r}{\lambda} + o\left(\frac{\lambda}{r}\right)\right], \\ &= F_0{}^2 \exp\left[-\frac{r^2}{\lambda\nu} + o\left(\frac{r^4}{\lambda\nu^3}\right)\right]. \end{aligned} \tag{17}$$

Our quantum *Ansatz* in Eq. (16) is parametrized with three parameters: the flux tube central intensity $F_0{}^2$, the flux tube damping measured by the penetration length $\lambda = 1/\mu$, and the flux tube central curvature radius $-2F_0{}^2/(\lambda\nu)$. For a simpler expression, we prefer to utilize the parameter ν instead of explicitly parametrizing the curvature.

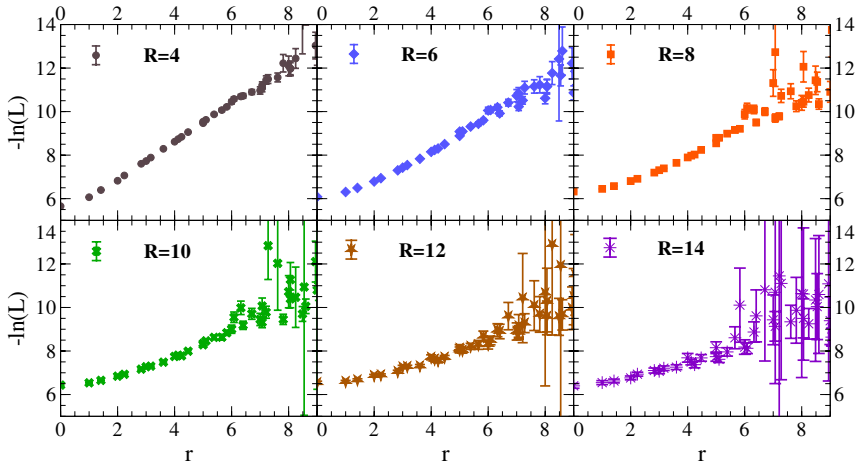

FIG. 7 (color online). Results for minus the log of the action density in the charge mediator plane for $R = 4$, $R = 6$, $R = 8$, $R = 10$, $R = 12$, and $R = 14$. The plots suggest the exponent is quadratic at small distances and linear at large distances, in agreement with our *Ansatz*.

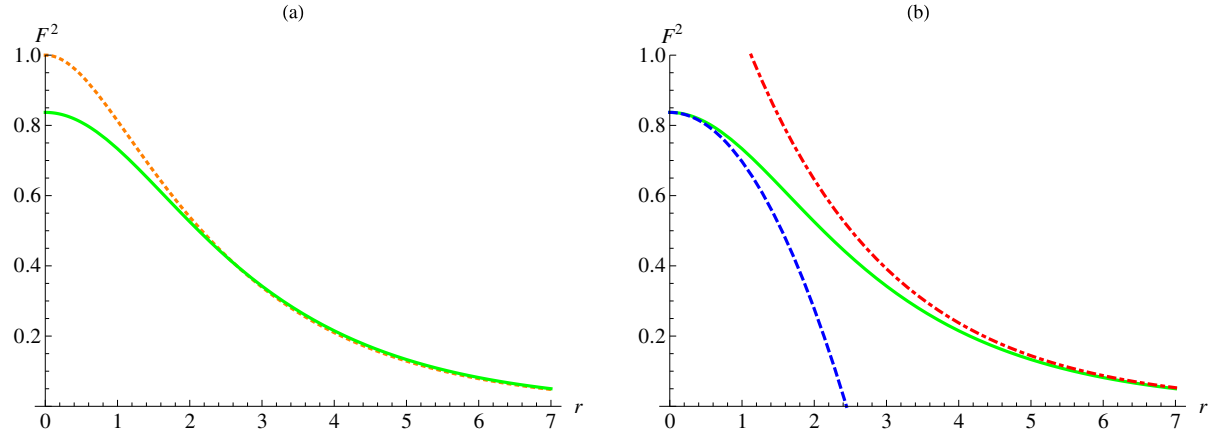

FIG. 8 (color online). In (a) we illustrate for arbitrary parameters $F_{0\mathrm{cl}}^2 = 1$, $\lambda = 1$, $\nu_{\mathrm{cl}} = 1$, $\alpha = 1$ our *Ansatz* for the classical flux tube profile (dashed line) and the quantum one (solid line) or convoluted one as a function of the distance to the charge axis r. In (b), the convoluted profile (solid line) and its large and small r asymptotic functions are shown. Our *Ansatz* for the quantum field is defined in Eq. (16).

Moreover, with our *Ansatz* ${F_{\mathrm{qu}}}^2(r)$ defined in Eq. (16), we obtain the following total width of the flux tube:

$$\omega = \sqrt{\frac{\int_0^\infty r^3 {F_{\mathrm{qu}}}^2(r)\,dr}{\int_0^\infty r {F_{\mathrm{qu}}}^2(r)\,dr}} = \sqrt{\frac{3}{2}\lambda^2 + 2\frac{\lambda\nu^2}{\lambda + 2\nu}}. \quad (18)$$

We now discuss how many characteristic distances can be extracted from fits of the flux tube profile measured with our lattice QCD data, which includes statistical error bars and is subject to statistical errors as well. The width ω is obtained with an integral for the squared components $F^2(r)$, and thus the error bars are averaged out; it is the clearest distance we can compute.

The parameters λ and ν are more sensitive to the details of our lattice QCD data. In the case where the signal is clear, such as the figures with smaller R in Fig. 7, λ and ν can be both determined with small error bars. However, at larger R, the two parameters λ and ν become redundant, and they are expected to have large error bars.

But we submit that further parameters are impossible to fit with the present lattice QCD data. For instance, the quantum widening α and the classical penetration length ξ would be interesting to measure, but they are difficult to separate. In confinement models where the electromagnetic fields are classical, the coherence length ξ is defined as the curvature of the field intensity in the center of the flux tube. The penetration length and the coherence length are characteristic of the medium (QCD in our case) where the flux tube resides, and they determine the string tension σ. For instance, the penetration length λ and the coherence length ξ are well defined in magnetic confinement models such as the Ginzburg-Landau model or the Ampère [38] equations or in the Bogoliubov–de Gennes equations [22]. However, the curvature at the center of the flux tube is also increased by the widening of the flux tube due to the zero mode quantum oscillations of the stringlike flux tube. The zero mode oscillations have a Gaussian shape of harmonic oscillator parameter α.

To illustrate this difficulty, let us convolute the classical flux tube profile with a Gaussian distribution typical of the quantum oscillation,

$$\phi^2(r) = \exp\left(-\frac{r^2}{\alpha^2}\right). \quad (19)$$

Notice this Gaussian already has a width of $\alpha/\sqrt{2}$. The result of the convolution is a quantum flux tube profile,

$${F_{\mathrm{qu}}}^2(r) = \int_0^\infty \int_0^{2\pi} \phi^2(r') {F_{\mathrm{cl}}}^2(\sqrt{r'^2 + r^2 - 2rr'\cos\theta}) d\theta r' dr'. \quad (20)$$

For simplicity, let us consider a typical classical flux tube profile ${F_{\mathrm{cl}}}^2(r)$ similar to our *Ansatz* for the quantum profile in Eq. (16) but with a classical parameter ν_{cl} related to the coherence length ξ. In Fig. 8, we illustrate the numerical result of this integration. We are able to compute analytically the profile ${E_{\mathrm{qu}}}^2(r)$ both close to the charge axis where the profile is quadratic in r,

$$\begin{aligned} {F_{\mathrm{qu}}}^2(r) = {F_{0\mathrm{cl}}}^2 &\left[1 - \frac{\alpha\sqrt{\pi}}{\lambda} e^{(\frac{\nu_{\mathrm{cl}}}{\alpha}+\frac{\alpha}{\lambda})^2} \mathrm{erfc}\left(\frac{\nu_{\mathrm{cl}}}{\alpha} + \frac{\alpha}{\lambda}\right)\right] \\ &\times \left\{1 - \left[-\frac{\alpha\lambda^2 + 2\lambda {\nu_{\mathrm{cl}}}^2 + 2\alpha^3}{\alpha\lambda^2} + \frac{2{\nu_{\mathrm{cl}}}^2 + \lambda\alpha}{\lambda\alpha}\right.\right. \\ &\left.\left. \times \frac{1}{1 - \frac{\alpha\sqrt{\pi}}{\lambda} e^{(\frac{\nu_{\mathrm{cl}}}{\alpha}+\frac{\alpha}{\lambda})^2} \mathrm{erfc}(\frac{\nu_{\mathrm{cl}}}{\alpha} + \frac{\alpha}{\lambda})}\right] \frac{r^2}{\alpha^2} + o\left(\frac{r^4}{\alpha^4}\right)\right\}, \end{aligned} \quad (21)$$

and at large distances from the charge axis where the penetration length dominates,

$$F_{\mathrm{qu}}{}^2(r) = F_{0\mathrm{cl}}{}^2 e^{\frac{2\lambda\nu_{\mathrm{cl}}+\alpha^2}{\lambda^2}} \exp\left[-\frac{2r}{\lambda} + o\left(\frac{\lambda}{r}\right)\right]. \quad (22)$$

These two asymptotic curves to the convolution are shown in Fig. 8. It is clear that the central curvature depends on both distance parameters ν_{cl} and α. Thus, it is not possible when error bars are nonvanishing to separate the classical coherence length ξ from the quantum widening $\alpha/\sqrt{2}$.

Importantly, the convoluted profile remains with a shape consistent with the *Ansatz* of Eq. (16), since it has both a finite curvature and an exponential decay. Moreover, the penetration length λ measured at the long-distance tail of the profile in r is unaffected by the convolution. Thus, λ constitutes an intrinsic characteristic distance [55] of SU(3) flux tubes.

In the rest of this paper, we utilize Eq. (16) to fit the profile $F_{\mathrm{qu}}{}^2(r)$ of the full quantum SU(3) flux tube in the mediator plane to determine the penetration length λ and to measure the widening $\omega(R)$.

B. In the planes of the two static charges

In the planes containing either the quark or the antiquark static charges, only one of the three characteristic distances of the QCD flux tube may be measured. The coherence length is masked by the charges, and the quantum widening only occurs in the flux tube. Thus, at most we may measure the screening of the Coulomb field; i.e., we can only measure the penetration length λ.

Nevertheless, for a more detailed study of the screening, we measure the fields in planes containing one of the two static charges. We compare our lattice data with three different models for the color fields. Without confinement, one has a simple Coulomb potential

$$F_{\mathrm{qu}}{}^2(r) = F_0{}^2 \frac{1}{r^4}, \quad (23)$$

when the distance to the charge r is smaller than the intercharge distance R. If confinement does produce a Yukawa-like screening, the color fields take the form

$$F_{\mathrm{qu}}{}^2(r) = F_0{}^2 \exp\left(\frac{-2r}{\lambda}\right)\left(\frac{\lambda r + 1}{r^2}\right)^2. \quad (24)$$

Finally, we may also consider a simple exponential screening similar to the one occurring in the mediator plane of the flux tube,

$$F_{\mathrm{qu}}{}^2(r) = F_0{}^2 \exp\left(\frac{-2r}{\lambda}\right), \quad (25)$$

where F_0 is just a normalization parameter.

Then it is important to check whether the penetration length λ measured in the plane of the charges is independent of the charge-anticharge distance R. For a simple picture of the screening of the color fields, we must also study if the penetration length λ measured in the planes of the charges coincides with the penetration length measured in the mediator plane.

Thus, we measure the color electric and color magnetic fields in planes including the charges. Because we consider long flux tubes, we choose to measure the color fields in the two planes parallel to the mediator plane. These planes are perpendicular to the z axis, and again the variable measuring the distance is $r = \sqrt{y^2 + z^2}$.

V. FITS OF THE FLUX TUBE PROFILES

A. The squared components of the electric and magnetic fields in both planes

Among all densities we measure, the Lagrangian or action density is the one with the strongest and clearest signal; therefore, this is the density we utilize to parametrize the profiles of the flux tube. Nevertheless, all the components squared of the electric and magnetic fields $E_z{}^2$, $E_r{}^2$, $E_\theta{}^2$, $B_z{}^2$, $B_r{}^2$, and $B_\theta{}^2$ are relevant to understand confinement.

In Fig. 9, we show that contrary to the dual superconductor models, all components of the fields are of the same order of magnitude inside the flux tube. Only close to the charges, the larger component is $E_z{}^2$ in the mediator plane and $E_\theta{}^2$ in the planes of the charges.

When the distance from the charges is sufficiently large, all the components $E_i{}^2 \sim 0.4$ and all the components $B_i{}^2 \sim -0.3$ in lattice spacing units. In any case, there is no dominant component of the color electric or magnetic fields. This is an important result that any model of confinement should address.

This also implies that, at sufficiently large distances from the charges, the parameter λ and the width w computed with any of our field densities are essentially the same.

B. Screening in the mediator plane

We find the noise increases with R, and thus we are able to compute the flux tube profiles only up to $R = 14a$. We think that our noise suppression techniques are nevertheless sufficient, since the lattice artifacts create larger systematic errors than the statistical noise, see Fig. 6. As a word of caution, we notice the systematic errors may contribute to increase the χ^2/d.o.f.

The fits of the profile of the flux tube in the mediator plane for the action density are shown in Fig. 10 and are listed in Table I. Notice we only consider in the error bars the statistical error, which increases with R, thus decreasing the χ^2/d.o.f. with R. In the smallest distance $R = 4$, the systematic errors are larger than the statistical errors, and the χ^2/d.o.f. is large. In the largest distances $R = 12$ and $R = 14$, the statistical errors are already large, and the profile parameters are not well determined. Nevertheless, we keep this distance in our study, since the error in the width of the flux tube remains small up to $R = 14$.

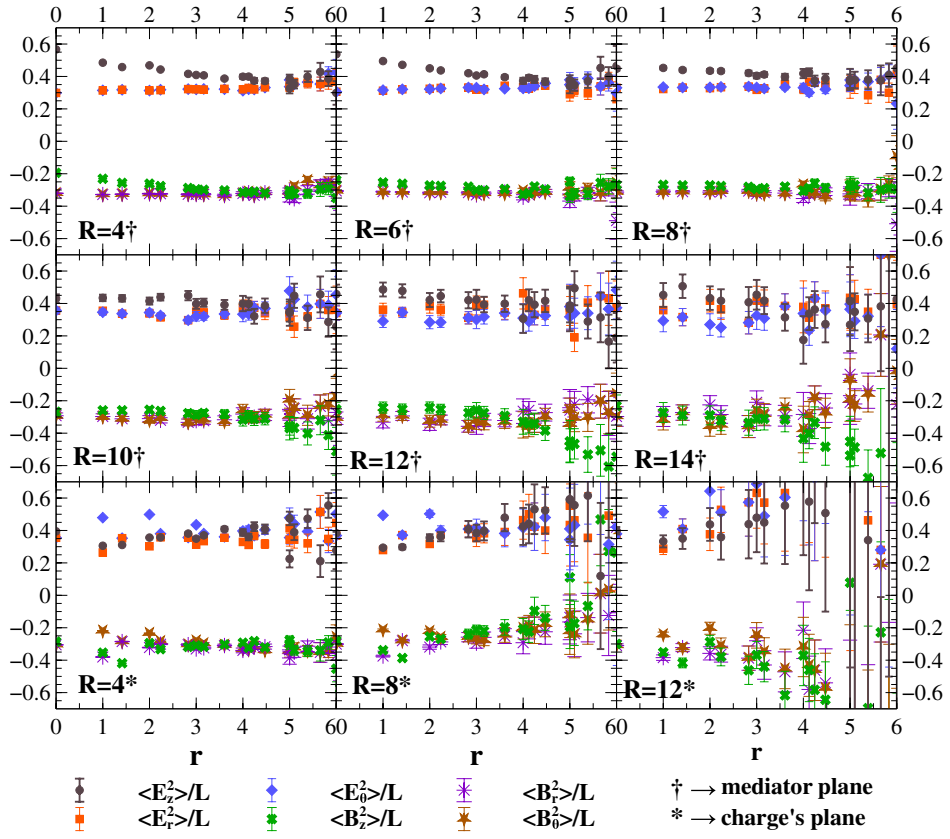

FIG. 9 (color online). Ratios of the components of the squared fields over the Lagrangian density for different intercharge distances R. We show the ratios both computed for the field profiles computed in the mediator plane of the color charges and in the planes of the color charges.

We remark that, although the other parameters change with R, the penetration length λ remains the same $\lambda \sim 2.2a$, or $\lambda \sim 0.22$ fm, within the statistical error bars. This unique scale for the penetration length is promising for the theoretical understanding of confinement.

The Lagrangian density in the center of the flux tube and for our largest R is of the order of 1.5×10^{-3} in dimensionless units. To arrive at physical dimensions, we have to multiply this by $2\beta/a^4 = 2.5 \times 10^4$ GeV fm^{-3}, and we arrive at a Lagrangian density of $\mathcal{L}_0 \sim 38$ GeV fm^{-3}.

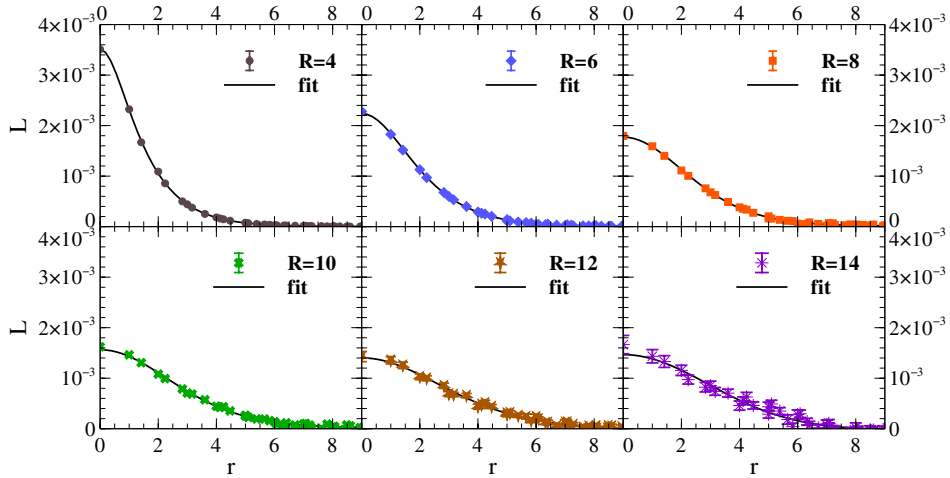

FIG. 10 (color online). Results for our fits to the profile of the action density in the mediator of the charges for $R = 4$, $R = 6$, $R = 8$, $R = 10$, $R = 12$, and $R = 14$.

TABLE I. Fits of the profile of the flux tube for the action density in the mediator plane for the longitudinal component. We also consider a constant shift of the density, very small and not shown here.

$R[a]$	$10^3\mathcal{L}_0$	$\lambda[a]$	$\nu[a]$	χ^2/d.o.f.
4	3.509 ± 26.72	2.165 ± 0.033	0.877 ± 3.335	4.086
6	2.236 ± 0.078	2.379 ± 0.156	2.04 ± 0.365	2.254
8	1.762 ± 0.023	2.052 ± 0.201	4.092 ± 20.22	1.999
10	1.549 ± 0.046	2.088 ± 0.536	5.306 ± 36.43	1.477
12	1.357 ± 0.051	0.913 ± 2.044	17.41 ± 200.1	1.055
14	1.491 ± 0.053	0.064 ± 0.018	268.0 ± 1392.4	1.331

C. Widening in the mediator plane

Since our *Ansatz* fits quite well the flux tube profile, we then utilize Eq. (18) to compute the width of the flux tube. Additionally, we compute the error bar or the width with the jackknife method. Our results for the width of the flux tube in the mediator plane are shown in Fig. 11. As can be seen, the tube flux becomes wider as the quark-antiquark distance is increased. We then fit the flux tube width with the leading-order one-loop computation in effective string theory [47] corresponding to the linear fit,

$$\omega^2 = A + B\log R. \tag{26}$$

The fit results in $A = 0.1477 \pm 0.0035$ fm^2 and $B = 0.0762 \pm 0.0090$ fm^2 with error bars computed with the jackknife method. We find a rather small χ^2/d.o.f. $= 0.383$.

The B parameter can be compared with the theoretical leading-order [47] value for the factor of the logarithmic term,

$$B = \frac{D-2}{2\pi\sigma} = 0.0640028 \text{ fm}^2 \tag{27}$$

obtained using a string tension of $\sqrt{\sigma} = 0.44$ GeV [74].

In what concerns the constant A parameter, it is possibly larger than the corresponding constant of the leading-order expansion of the string theory, due to the intrinsic width of the flux tube. The QCD flux tube is not tachyonic and its width is always real and positive. Notice a simple exponential profile according to Eq. (18) already leads for very small distances to $w^2 = 3\lambda^2/2 \sim 0.07$ fm^2. Indeed this is similar to the width we get at our smaller distance of $R = 4a \simeq 0.4$ fm.

Notice that the error bars of the fit of the width are much smaller that the error bars for the parameters λ and ν at larger intercharge distance R shown in Table I. This is expected since at larger R, the profile error bars are larger and the two parameters λ and ν become redundant. As for

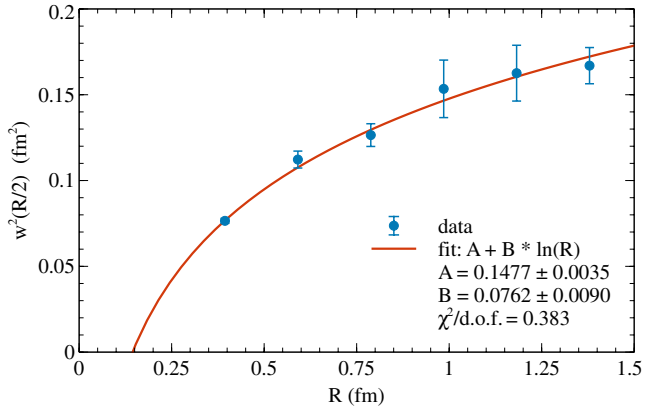

FIG. 11 (color online). Square of the width of the flux tube $w^2 = \langle r^2\rangle$ in the mediator plane computed with our *Ansatz*. The error bars are determined with the jackknife method. The solid line corresponds to the fit of the widening of the quantum string.

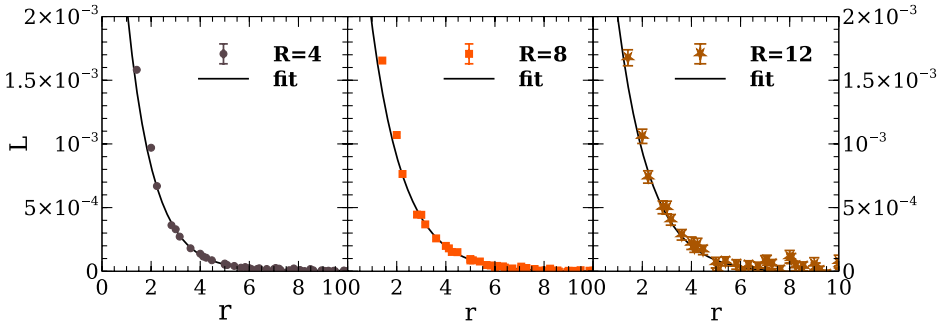

FIG. 12 (color online). Lattice QCD data and fits with the exponential decay *Ansatz* for the profile of the action density in the planes of the charges shown for $R = 4$, $R = 8$, and $R = 12$.

TABLE II. Parameters of the fits to the profile of the flux tube for the action density in the planes of the charges. We also consider a constant shift of the density, very small and not shown here.

$R[a]$	$10^3\,\mathcal{L}_0$	$\lambda[a]$	χ^2/d.o.f.
4	5.3412 ± 17.2634	2.1315 ± 0.1257	6.5385
6	4.4985 ± 14.7985	2.4516 ± 0.1512	2.258
8	4.1122 ± 13.2691	2.6399 ± 0.1281	0.8602
12	4.2334 ± 25.2801	2.6804 ± 0.4002	1.8935

the width ω, an integral over all profile points, the impact of the profile error bars is smaller. Nevertheless, because the parameters λ and ν of our *Ansatz* show large error bars for the intercharge distances of $R = 14$ and $R = 12$, we repeat the fit removing these two points. We get essentially the same result for the fit parameters A and B and for the χ^2/d.o.f. with five, six, and seven points. Thus, our fit is quite stable.

To comply exactly with the quantum widening of an infinitely thin string, the string should be much thinner than longer, and also much thinner than the width of the quantum vibrations. Indeed we have $R \gg \lambda$, however, $w \sim \lambda$. A very interesting result already is that our fitted factor to the logarithm is close to one standard deviation from the theoretical one-loop result, considering a large part or the width is due to the penetration length.

D. Screening in the planes of the two static charges

We find that only one of the three *Ansätze* in Eqs. (23)–(25) fits correctly the action density in the planes of the charges. Both the Coulomb and Yukawa fields produce very poor fits of our lattice data for the fields. A poor fit by the Coulomb *Ansatz* was expected since a flux tube is consistent with color screening. However, the Yukawa *Ansatz* also leads to a poor fit, and this indicates that the screening occurring in confinement differs from a Yukawa screening.

Importantly, the exponential *Ansatz* fits correctly the tail of the fields in the planes of the charges, see Fig. 12. Thus, we have screening, though it is not a Yukawa screening. Moreover, the fit results in a parameter $\lambda \sim 0.22$ to 0.24 fm, as listed in Table II. The λ fitted in the planes of the charges is consistent with the λ obtained in the mediator plane to the charges.

VI. CONCLUSIONS

We compute the quark-antiquark flux tube in pure gauge SU(3) lattice QCD. We measure the profile of the electric and magnetic field densities both in the mediator plane of the color charges and in the planes of the charges. We utilize three complementary techniques to enhance the signal-to-noise ratio and are able to reduce the statistical noise below the systematic errors of our lattice setup.

We show the flux tube is due to screening of the electric and magnetic field components, since we measure a penetration length $\lambda \sim 0.22$ to 0.24 fm. The inverse of λ may indicate an effective screening mass, possibly for the gluon or dual gluon, of $\mu \sim 0.8$ to 0.9 GeV. Moreover, the same screening parameter is universal in the sense it occurs in all components squared of the electric and magnetic fields ${E_z}^2$, ${E_r}^2$, ${E_\theta}^2$, ${B_z}^2$, ${B_r}^2$, and ${B_\theta}^2$, both in the mediator plane and in the charge's plane.

However, there are differences to the dual superconductor models. The vector electric and magnetic fields are not gauge invariant; their squared components are the first gauge-invariant function of the field components. Moreover, all the squared components have the same order of magnitude and essentially similar profiles; thus, the longitudinal color electric field is not dominant.

Importantly, this allows us to use the Lagrangian density, since it has the largest signal-to-noise ratio, to determine the width of the flux tube up to a distance of 14 lattice spacings. We find that the width complies almost within one standard deviation with the logarithmic widening obtained at leading order in the Nambu-Gotto effective string theory.

Our results lead to a better understanding of the nature of the confining SU(3) flux tube. We hope this work will motivate more lattice QCD studies of flux tubes and will be useful for the theoretical understanding both of the QCD confinement and of string theory.

ACKNOWLEDGMENTS

We thank Martin Lüscher, Uwe-Jens Wiese, and Pedro Sacramento for enlightening discussions on flux tubes. This work was supported by Portuguese national funds through FCT - Fundação para a Ciência e Tecnologia, Projects No. PEst-OE/FIS/UI0777/2011, No. CERN/FP/116383/2010, and No. CERN/FP/123612/2011. We also acknowledge NVIDIA support with an Academic Partnership Program and a CUDA Teaching Center Program.

[1] A. Di Giacomo, M. Maggiore, and S. Olejnik, Phys. Lett. B **236**, 199 (1990).
[2] A. Di Giacomo, M. Maggiore, and S. Olejnik, Nucl. Phys. **B347**, 441 (1990).
[3] V. Singh, D. Browne, and R. Haymaker, Phys. Lett. B **306**, 115 (1993).
[4] G. Bali, K. Schilling, and C. Schlichter, Phys. Rev. D **51**, 5165 (1995).

[5] T. Regge, Nuovo Cimento **14**, 951 (1959).
[6] T. Regge, Nuovo Cimento **18**, 947 (1960).
[7] P. D. B. Collins, *An Introduction to Regge Theory and High Energy Physics*, (Cambridge University Press, Cambridge, England, 1977).
[8] A. B. Kaidalov, arXiv:hep-ph/0103011.
[9] D. Bugg, Phys. Rep. **397**, 257 (2004).
[10] M. Cardoso, N. Cardoso, and P. Bicudo, Phys. Rev. D **81**, 034504 (2010).
[11] N. Cardoso, M. Cardoso, and P. Bicudo, Phys. Rev. D **84**, 054508 (2011).
[12] N. Cardoso, M. Cardoso, and P. Bicudo, Phys. Lett. B **710**, 343 (2012).
[13] M. Cardoso, N. Cardoso, and P. Bicudo, Phys. Rev. D **86**, 014503 (2012).
[14] N. Cardoso and P. Bicudo, Phys. Rev. D **87**, 034504 (2013).
[15] Y. Nambu, Phys. Rev. D **10**, 4262 (1974).
[16] G.'t Hooft, Nucl. Phys. **B153**, 141 (1979).
[17] S. Mandelstam, Phys. Rep. **23**, 245 (1976).
[18] M. Baker, J. S. Ball, and F. Zachariasen, Phys. Rev. D **41**, 2612 (1990).
[19] M. Baker, J. S. Ball, and F. Zachariasen, Phys. Rep. **209**, 73 (1991).
[20] A. A. Abrikosov, Sov. Phys. JETP **5**, 1174 (1957).
[21] H. B. Nielsen and P. Olesen, Nucl. Phys. **B61**, 45 (1973).
[22] M. Cardoso, P. Bicudo, and P. D. Sacramento, Ann. Phys. (Amsterdam) **323**, 337 (2008).
[23] A. M. Polyakov, Phys. Lett. **59B**, 82 (1975).
[24] T. Banks, R. Myerson, and J. B. Kogut, Nucl. Phys. **B129**, 493 (1977).
[25] J. Smit and A. van der Sijs, Nucl. Phys. **B355**, 603 (1991).
[26] G. S. Bali, V. Bornyakov, M. Muller-Preussker, and K. Schilling, Phys. Rev. D **54**, 2863 (1996).
[27] F. Gubarev, E.-M. Ilgenfritz, M. Polikarpov, and T. Suzuki, Phys. Lett. B **468**, 134 (1999).
[28] Y. Koma, M. Koma, E.-M. Ilgenfritz, T. Suzuki, and M. Polikarpov, Phys. Rev. D **68**, 094018 (2003).
[29] M. Chernodub, K. Ishiguro, Y. Mori, Y. Nakamura, M. Polikarpov, T. Sekido, T. Suzuki, and V. Zakharov, Phys. Rev. D **72**, 074505 (2005).
[30] Y. V. Burdanov, G. V. Efimov, and S. N. Nedelko, arXiv:hep-ph/9806478.
[31] D. Jia, arXiv:hep-th/0509030.
[32] T. Suzuki, K. Ishiguro, Y. Mori, and T. Sekido, AIP Conf. Proc. **756**, 172 (2005).
[33] H. Suganuma, K. Amemiya, H. Ichie, and Y. Koma, arXiv:hep-ph/0407121.
[34] H. Suganuma *et al.*, arXiv:hep-lat/0407020.
[35] H. Suganuma and H. Ichie, Nucl. Phys. B, Proc. Suppl. **121**, 316 (2003).
[36] A. Kumar and R. Parthasarathy, Phys. Lett. B **595**, 373 (2004).
[37] J. V. Burdanov and G. V. Efimov, arXiv:hep-ph/0209285.
[38] N. Cardoso, M. Cardoso, and P. Bicudo, arXiv:1004.0166.
[39] O. Oliveira and P. Bicudo, J. Phys. G **38**, 045003 (2011).
[40] P. Bicudo, F. Giacosa, and E. Seel, Phys. Rev. C **86**, 034907 (2012).
[41] M. S. Cardaci, P. Cea, L. Cosmai, R. Falcone, and A. Papa, Phys. Rev. D **83**, 014502 (2011).
[42] P. Cea, L. Cosmai, and A. Papa, Phys. Rev. D **86**, 054501 (2012).
[43] Y. Nambu, Phys. Lett. **80B**, 372 (1979).
[44] T. Goto, Prog. Theor. Phys. **46**, 1560 (1971).
[45] M. Luscher, G. Munster, and P. Weisz, Nucl. Phys. **B180**, 1 (1981).
[46] J. Arvis, Phys. Lett. **127B**, 106 (1983).
[47] F. Gliozzi, M. Pepe, and U.-J. Wiese, J. High Energy Phys. 11 (2010) 053.
[48] A. Amado, N. Cardoso, M. Cardoso, and P. Bicudo, Acta Phys. Pol. B **5**, 1129 (2012).
[49] A. Armoni and J. M. Ridgway, Nucl. Phys. **B801**, 118 (2008).
[50] V. Bornyakov, A. Kovalenko, M. Polikarpov, and D. Sigaev, Nucl. Phys. B, Proc. Suppl. **119**, 739 (2003).
[51] V. Bornyakov, A. Kovalenko, M. Polikarpov, and D. Sigaev, Nucl. Phys. B, Proc. Suppl. **129–130**, 757 (2004).
[52] M. Cardoso, P. Bicudo, and N. Cardoso, Acta Phys. Pol. B **5**, 1149 (2012).
[53] M. Caselle, F. Gliozzi, U. Magnea, and S. Vinti, Nucl. Phys. **B460**, 397 (1996).
[54] M. Caselle, J. High Energy Phys. 08 (2010) 063.
[55] M. Caselle and P. Grinza, J. High Energy Phys. 11 (2012) 174.
[56] M. Chernodub and F. Gubarev, Phys. Rev. D **76**, 016003 (2007).
[57] P. Giudice, F. Gliozzi, and S. Lottini, Proc. Sci., LAT2006 (2006) 070.
[58] P. Giudice, F. Gliozzi, and S. Lottini, J. High Energy Phys. 01 (2007) 084.
[59] F. Gliozzi, arXiv:hep-lat/0601011.
[60] F. Gliozzi, arXiv:hep-lat/9410022.
[61] F. Gliozzi, M. Pepe, and U.-J. Wiese, J. High Energy Phys. 01 (2011) 057.
[62] F. Gliozzi, M. Pepe, and U.-J. Wiese, Phys. Rev. Lett. **104**, 232001 (2010).
[63] J. Greensite and P. Olesen, J. High Energy Phys. 11 (2000) 030.
[64] B. Lucini and M. Teper, Phys. Rev. D **64**, 105019 (2001).
[65] H. B. Meyer, Phys. Rev. D **82**, 106001 (2010).
[66] A. Bakry, D. Leinweber, P. Moran, A. Sternbeck, and A. Williams, Phys. Rev. D **82**, 094503 (2010).
[67] A. S. Bakry, D. B. Leinweber, and A. G. Williams, Phys. Rev. D **85**, 034504 (2012).
[68] P. Bicudo, M. Cardoso, and O. Oliveira, Phys. Rev. D **77**, 091504 (2008).
[69] M. Cardoso, P. Bicudo, and O. Oliveira, Proc. Sci., LAT2007 (2007) 293.
[70] K. G. Wilson, Phys. Rev. D **10**, 2445 (1974).
[71] M. Creutz, *Quarks, Gluons and Lattices* (Cambridge University Press, Cambridge, England, 1984).
[72] C. Gattringer and C. B. Lang, Lect. Notes Phys. **788**, 1 (2010).
[73] N. Cardoso and P. Bicudo, Comput. Phys. Commun. **184**, 509 (2013).

[74] R. Edwards, U. M. Heller, and T. Klassen, Nucl. Phys. **B517**, 377 (1998).
[75] R. Brower, P. Rossi, and C.-I. Tan, Nucl. Phys. **B190**, 699 (1981).
[76] G. Parisi, R. Petronzio, and F. Rapuano, Phys. Lett. **128B**, 418 (1983).
[77] M. Luscher and P. Weisz, J. High Energy Phys. 09 (2001) 010.
[78] M. Falcioni, M. Paciello, G. Parisi, and B. Taglienti, Nucl. Phys. **B251**, 624 (1985).
[79] M. Albanese *et al.* (APE Collaboration), Phys. Lett. B **192**, 163 (1987).
[80] M. Luscher and U. Wolff, Nucl. Phys. **B339**, 222 (1990).
[81] C. R. Allton, C. T. Sachrajda, and C. Michael (UKQCD Collaboration), Phys. Rev. D **47**, 5128 (1993).